JOURNAL OF GEOPHYSICAL RESEARCH, VOL. 102, NO. C1, PAGES 1073–1089, JANUARY 15, 1997

Internal waves and tides in the western Weddell Sea: Observations from Ice Station Weddell

Murray D. Levine and Laurie Padman

College of Oceanic and Atmospheric Sciences, Oregon State University, Corvallis

Robin D. Muench

Earth and Space Research, Seattle, Washington

James H. Morison

Polar Science Center, Applied Physics Laboratory, College of Ocean and Fishery Sciences
University of Washington, Seattle

Abstract. The upper ocean current and temperature fields in the western Weddell Sea were measured from the drifting pack ice at Ice Station Weddell 1 (ISW) and nearby sites using a vertical profiler and an array of moored sensors in January–June 1992. These data document the structure and variability of the internal gravity wave field and tidal currents in this remote region. The variance of the internal wave continuum ($f <$ frequency $< N$) at ISW was 0.2–0.6 of the Garrett-Munk (GM) universal level for the first 60 days, increasing to near GM levels during the final 10 days of the deployment. In contrast, the energy density at site C, 50 km west of ISW and farther up the continental slope, was always near GM levels. Variations may be due to a combination of spatial and temporal gradients of the internal wave field. At ISW, coherence between vertically separated sensors was used to estimate vertical wave number bandwidth. Energy and bandwidth estimates are compared with previous studies in both ice-covered and temperate oceans. Using our measurements of the internal wave field and existing parameterizations of mixing, we estimate the vertical heat flux from the Warm Deep Water toward the surface. At ISW the upward heat flux due to mixing associated with the internal waves was about 1 W m^{-2}, much less than the 20 W m^{-2} average flux required to balance the heat budget for the Weddell Gyre. Tidal currents contributed significantly to the total measured horizontal velocity variance. The tides were primarily barotropic and increased toward the west in both the semidiurnal and diurnal frequency bands. It is suggested that the stronger tidal currents to the west, over the shallower water of the upper continental slope, are indirectly responsible for the higher internal wave energy at site C relative to ISW.

1. Introduction

Internal gravity waves are a natural mode of oscillation in a stratified fluid. Early theoretical formulations were derived by *Stokes* [1847] for a two-layer fluid and *Rayleigh* [1888] for continuous stratification. Published observations of geophysical internal waves followed soon after the turn of the century (see *Munk* [1981] for a more complete historical perspective). The mere presence of internal waves indicates that the ocean is not in complete equilibrium. As with any wave motion, internal waves are radiated in response to time-dependent forcing that perturbs the local equilibrium state. Waves transport momentum and energy, leaving in their wake a new equilibrium state.

It is useful for this discussion to divide internal waves into three components according to frequency: near-inertial waves, baroclinic tides, and an internal wave "continuum". Near-inertial waves are strongly influenced by the rotation of the Earth and oscillate at a frequency near the local inertial frequency f. These waves are often generated by wind forcing. The diurnal and semidiurnal tidal frequency bands may contain both barotropic and internal waves. While the barotropic tide is generated directly by astronomical forcing, internal tides are internal waves that are generated by the interaction of the barotropic tide with topography. The internal wave "continuum" refers to the relatively smooth spectrum of waves between f and N, the frequency band for freely propagating waves.

Paper number 96JC03013.
0148-0227/97/96JC-03013$09.00

The climatology of each of these three components is different. Near-inertial waves vary considerably in time and space and, in the upper ocean, are often associated with specific storm-forcing events. The internal tide is found throughout the world ocean and usually contains a significant fraction of the total internal wave energy. Unlike the regularity of the barotropic tide, the amplitude and phase of the internal tide are variable in time: no universal model exists for their prediction. In contrast to the other components, the background continuum has been found to be relatively steady in time and homogeneous in space. This remarkable realization was first discussed by *Garrett and Munk* [1972]. Internal waves are as "common as waves at the sea surface–perhaps even more so, for no one has ever reported an interior calm" [*Munk,* 1981, p. 264]. The constancy of the wave field has made identification of sources and sinks of internal waves difficult. Waves are apparently generated from many locations and then fill the ocean by propagating horizontally and vertically before being dissipated. The observed horizontal isotropy of the wave field provides evidence that the waves exist for enough time to produce a fairly random sea, making identification of the start and end of wave packets difficult. Also, tracking individual wave packets is further complicated by the possible nonlinear interaction among waves. Eventually, all internal waves are dissipated, their energy undoubtedly contributing to mixing the ocean. In the deep ocean this random sea can be described by the empirical statistical formulation known as the Garrett-Munk (GM) spectrum [*Garrett and Munk,* 1972, 1975; *Munk,* 1981]. The GM spectrum has been shown to be a reliable first-order description of the wave field throughout the world's oceans.

In interpreting observations it must be realized that other processes may contribute to oceanic variability at the space scales and timescales often dominated by internal waves and tides. Sometimes these processes are collectively referred to as irreversible fine structure to be distinguished from the reversible nature of linear waves [e.g., *Desaubies and Gregg,* 1981; *Lien and Müller,* 1992]. Many different phenomena may actually be responsible for generating fine structure. Density and velocity fine structure may be a signature of mixing, intrusions, vortical modes, or mesoscale processes. Waves may then advect the fine structure, greatly obscuring the interpretation of observations.

While there is much statistical similarity among the internal wave fields in different regions, there are some differences. Relating differences in the wave field to differences in the oceanic environment and external forcing may help identify the important sources and sinks of the waves [*Wunsch,* 1975]. Progress toward understanding internal wave dynamics comes from the synthesis of observations made at these different locations under a variety of conditions.

This paper reports on observations of internal waves and tides in the western Weddell Sea, an area of the ocean that has seldom been explored. In 1992 a joint U.S./Russian ice camp named Ice Station Weddell 1 (ISW) was established in this region (see *Gordon et al.* [1993a] for an overview of the project). The area is perennially covered by thick, drifting pack ice which has limited access by researchers. ISW provided a stable, slowly drifting platform which permitted the deployment of instruments capable of recording high-frequency time series.

We first describe the high-frequency and tidal oscillations of the temperature and velocity fields in the upper ocean during the ISW drift. These observations are interpreted within the framework of the three components of the wave field. Spectral analysis of the continuum permits a close comparison with the GM formulation and with data from previous studies. Variations of the wave field as a function of time and space are described. Using the measured internal wave field and existing empirical relationships, we estimate the turbulent dissipation rate and the associated heat flux. Implications for the regional heat balance are discussed. The current meter data are analyzed using traditional tidal analysis, and the cross-slope variability is discussed and compared with a numerical tidal model.

2. Experiment Description

Measurements were made at ISW from late January to early June 1992. During this time the ice station drifted about 600 km northward from 52°W, 71.5°S to 52°W, 66°S (Figure 1). The detailed drift track was determined by Global Positioning System (GPS) satellite navigation. The average drift speed was 0.10 m s^{-1}, and peak values approached 0.35 m s^{-1}. (In this paper, time is expressed as day of year (DOY) 1992 (UT), where DOY 1.0 is 0000 on January 1.)

Time series of temperature profiles in the upper ocean provided the primary observations for the detection of internal waves at ISW. These data were obtained from an ice-anchored mooring using 14 self-contained miniature data recorders (MDRs; Alpha Omega Computer Systems) [*Robertson et al.,* 1995] that recorded temperature every 2 min. An additional MDR at the bottom of the mooring recorded pressure as well as temperature at 4-min sampling. The measured pressure and a simple analytical model of the mooring dynamics in a uniform ice-relative flow were used to estimate the depth of each sensor as the mooring responded to the current drag. Sensors were located at nominal depths (i.e., the depth when the mooring line was vertical) between 12.5 and 290 m. The MDRs located at 130, 160, 190, 220, 250, and 290 m were used in this analysis. At shallower depths the temperature gradient was too variable to infer vertical displacement. The resolution of the MDRs was about 0.003°C in temperature and 0.3 m in pressure. The temperature time series were converted to vertical displacement using the local, 12-hour averaged vertical temperature gradient estimated from adjacent MDRs.

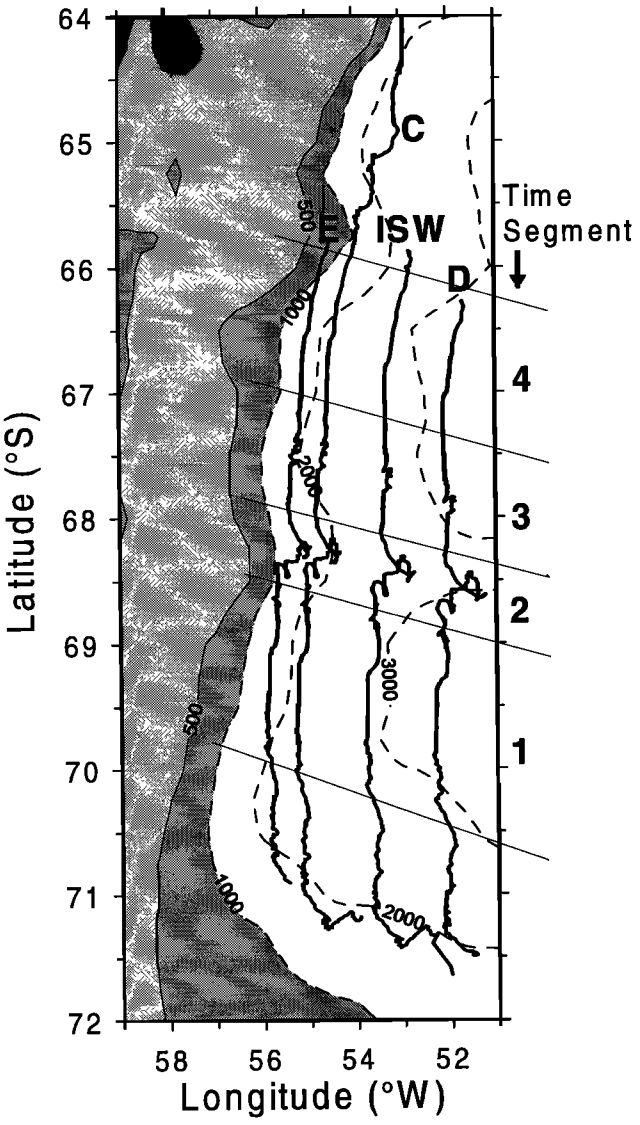

Figure 1. Drift tracks (bold lines) for Ice Station Weddell 1 (ISW) and remote mooring sites C, D, and E. Isobaths (dashed lines) are based on *LaBrecque and Ghidella* [1993] and measurements made from the main camp and helicopter CTD transects during the experiment. Water depths less than 1000 m are shaded. The approximate edge of the continental shelf is near the 500-m isobath.

A second mooring at ISW supported smart acoustic current meters (SACMs; Neil Brown, Inc.) at 50- and 200-m depth, which obtained hourly vector-averaged samples for the duration of the station [*Muench and Gordon,* 1995]. Similar moorings were also deployed east and west of ISW at sites C, D, and E (Figure 1). Absolute velocity was obtained by removing the measured ice drift velocity from the recorded time series. The drift velocity is based on a smoothed fit to the GPS position estimates using the method of *McPhee* [1988]. In this method, ice motion is assumed to consist entirely of a mean plus tidal and inertial components; a best fit is made using 2-day sections of the ice position data. Errors in the fit are due to data errors and ice motion at frequencies not included in the fit. The procedure is described in more detail by *Muench and Gordon* [1995].

Internal waves were also observed at site C with a Polar Ocean profile (POP) buoy. The buoy measured temperature and conductivity every 12 min at nominal depths of 10, 40, 70, 120, 200, and 300 m with SeaCat SBE-16 temperature-conductivity recorders (Sea-Bird Electronics). Data were telemetered through the Argos system along with buoy position. The SeaCats at 40, 120, and 300 m were equipped with pressure sensors to measure the true depth of the sensor array. A cable model was used to estimate the actual depths of the other recorders nominally at 10, 70, and 200 m. Frequent deflection of the cable due to currents or ice motion allowed each sensor package to sample a region of the water column above its nominal depth. To estimate the vertical displacement of the water, the temperature, salinity, and density data were first divided into 2-day groups. Nonparametric curve fits [*Steele and Morison,* 1992] produced representative, smooth profiles for each variable at every 10 m of depth. The smooth density profiles provided estimates of N^2. Using the 200-m sensor, the high-frequency deviations from the 2-day average profiles were used to estimate vertical-displacement time series for both temperature and density.

The displacements inferred from density variation were much noisier than those estimated from temperature, since density gradients were often small relative to the temperature gradients. Consequently, we use only the displacements derived from temperature. When cable motion was particularly large or temperature gradients were particularly small, the uncertainty in the displacement estimate was increased. For the sensor at 200 m we quantify this with an error criterion, $E = d^2 + [0.01°C/(dT/dz)]^2$, where d^2 is the variance of the depth of the sensor at 200 m and dT/dz is the estimated temperature gradient at 200 m. The 0.01°C is the practical accuracy of the temperature measurement. Displacement estimates are unreliable for relatively large values of E.

The vertical structure of the internal wave field was also investigated using temperature measurements made with the rapid-sampling vertical profiler (RSVP). About 700 profiles were obtained from the surface to 350-m depth. The main purpose of the RSVP was to resolve the scales of temperature and velocity shear that are required to infer turbulent dissipation and mixing rates: a discussion of these results and a description of the RSVP are given by *Robertson et al.* [1995].

The background stratification at ISW was determined from profiles of conductivity and temperature made with a conductivity-temperature-depth recorder (CTD) about every 10 km along the track [*Gordon et al.,* 1993a, b; *Muench and Gordon,* 1995]. An acoustic pinger on the CTD was used to determine water depth under the ice station at the time of each cast; cross-slope topography was also measured during helicopter CTD surveys.

3. Observations and Theoretical Considerations

We consider separately the internal wave continuum, near-inertial, and tidal frequency bands. At the latitude of ISW the frequencies of the semidiurnal tide and near-inertial oscillations are very close, and it is not possible to separate them. Nevertheless, it appears that there was very little energy at ISW that can be attributed to near-inertial motions, as there was no evidence of generation caused by the acceleration of the ice cover during several storms, even at the shallower current meter depth of 50 m. Hence the semidiurnal band appears to be dominated by the tide. We argue that the observed semidiurnal tide is primarily barotropic as the internal tide would probably show a greater difference between tidal current ellipses at 50 and 200 m than was observed.

3.1. Continuum Internal Waves

3.1.1. Theoretical considerations. To facilitate a comparison of the continuum wave field with other observations, a common framework is needed. The Garrett-Munk spectrum has served as a standard for this purpose for the past 20 years. Since it was first published, variations and alternative formulations have been proposed, including modifications by Garrett and Munk themselves. To simplify and clarify the discussion, it is useful to focus on the essential features of the GM spectrum and to extract the most fundamental quantities for comparison with other observations. This approach permits consistent comparison among diverse spectral formulations and focuses the discussion on physically meaningful quantities. The essential tenets of the GM spectrum are that the internal wave field is a linear sum of random internal waves that obey the dispersion relation and is stationary in time and homogeneous in the horizontal. The wave field is also homogeneous in the vertical after the energy is scaled by $N(z)$ (WKB approximation).

In constructing such a spectral model, spectral shapes in frequency and wave number are chosen that best represent the data. Using the spectral shapes consistent with GM, the internal wave field can be described using only two independent parameters, r and t, that describe energy and wave number bandwidth, respectively [*Desaubies,* 1976]. More parameters in more complicated spectral models can be constructed, but this two-parameter formulation allows an informative first-order intercomparison of wave fields. The specific spectral formulations used in this paper are given in the Appendix.

Using the GM formulation and notation given in *Munk* [1981] (known as GM79) the two parameters become

$$\begin{aligned} r_{\mathrm{GM79}} &= Eb^2N_0 \\ &= 0.56[\mathrm{m^2s^{-1}}] \\ t_{\mathrm{GM79}} &= \frac{j_*\pi}{bN_0} \\ &= 1.39[\mathrm{m^{-1}s}] \end{aligned} \tag{1}$$

where we use the GM79 values of the parameters: $b = 1300$ m (vertical stratification scale), $N_0 = 3$ cph ("surface" N), $j_* = 3$ (number of equivalent vertical modes), and $E = 6.3 \times 10^{-5}$ (nondimensional energy scale). The two parameters, r and t, essentially replace the four GM parameters E, b, N_0, and j_* without any loss of generality. The total energy of the wave field over all frequencies and wave numbers (J kg^{-1}) can be expressed as $E_{\mathrm{tot}} = rN$. Therefore the levels of the frequency and wave number spectra (A1), (A2), and (A7) are also proportional to r. In addition, $S(\omega)$ depends on f, although this does not appear to be an accurate reflection of observations, especially at low latitudes. *Munk* [1981] suggested that perhaps a constant value for f, say f at 30° latitude, should be used instead. However, to facilitate comparisons between our observations and GM79, we retain the f dependence in (A1) and (A2).

The parameter t sets the wave number bandwidth of the wave field and thereby describes the coherence structure: the more wave numbers that are present at a given frequency, the lower the coherence will be. In order to compare model formulations with different spectral shapes, it is convenient to define an "equivalent" vertical wave number bandwidth β_e as the wave number bandwidth of an equivalent rectangular distribution function with the same ratio of variance to squared mean. This definition has been used previously for comparing internal wave observations [e.g., *Müller et al.,* 1978; *Katz and Briscoe,* 1979; *Levine,* 1990]. For GM79, $\beta_e = \pi t N(z)$. Note that the vertical wave number bandwidth can also be associated with a horizontal wave number bandwidth α_e through the dispersion relation

$$\alpha_e = \beta_e \left(\frac{\omega^2 - f^2}{N^2 - \omega^2} \right)^{1/2} \tag{2}$$

where ω is the frequency.

3.1.2. Observations at ISW. In this section the continuum internal wave field observed at ISW is described and compared with the GM spectrum. Observations from site C are discussed in section 3.1.3.

To examine the temporal variability of the internal wave continuum, the variance at one depth is plotted as a function of time (Figure 2). Variance is shown for frequency bands from 0.1 to 0.8 cph for vertical displacement and from 0.15 to 0.35 cph for horizontal velocity. The frequency band limits have been chosen to avoid oscillations near f ($\approx$0.08 cph) which may

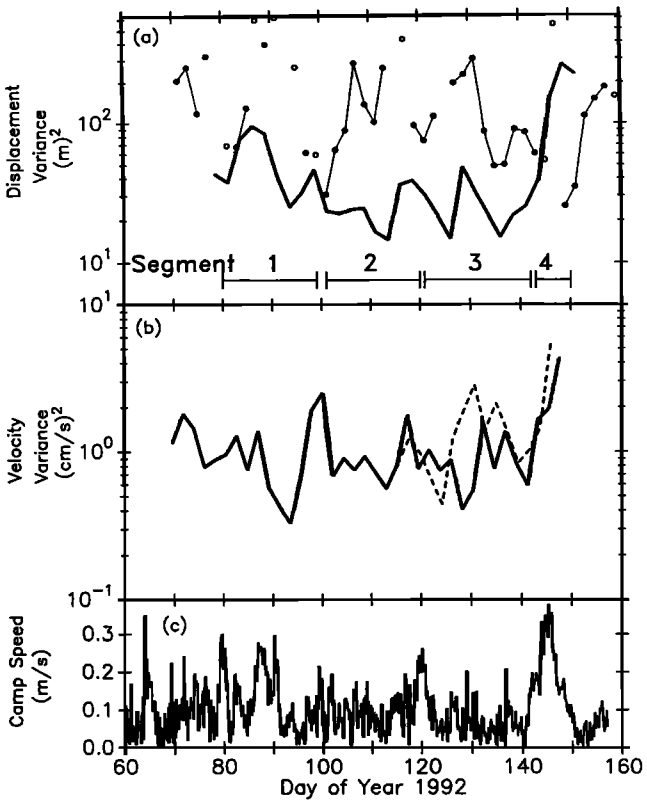

Figure 2. (a) Variance of vertical displacement (0.1 to 0.8 cph) at ISW at 250 m (bold line) and at site C at 200 m (solid circles for $E < 30m^2$; open circles for $E > 30m^2$). (b) Variance of horizontal velocity (0.15 to 0.35 cph) at ISW (solid line) and site C (dashed line) at 200 m. (c) The along-track speed of ISW.

be confused with the semidiurnal tide. The resolved frequency bandwidth of horizontal velocity was smaller than vertical displacement due to the lower Nyquist frequency (0.5 cph) for hourly data. The vertical displacement variance is estimated from the MDR at a nominal depth of 250 m. The vertical temperature gradient at this depth was the most stable for any of the sampled depths and therefore permits the best estimates of vertical displacement. The horizontal velocity variance is from the current meter at 200 m.

On the basis of the variations in background stratification and bottom topography, it is convenient to divide the time series into four segments (Figures 1 and 3):

1. During segment 1 (DOY 80 through 99), the ice station was located over the central continental slope in water 2500 to 3000 m deep. A shallow (30 to 50 m), weak seasonal pycnocline was present. Ice drift was steadily northward.

2. During segment 2 (DOY 101 through 120), the ice drift velocity was more variable and the seasonal pycnocline was weaker than in segment 1. *Muench and Gordon* [1995] identify this segment as a period of pronounced westward geostrophic flow, compared with the predominantly northward flow before and after this period. The variability in the drift at this time was consistent with the ice motion being forced primarily by the wind stress, which was also highly variable during this period.

3. During segment 3 (DOY 121 through 143), the ice station was again over the central continental slope and traveling northward. The seasonal pycnocline was now absent.

4. During segment 4 (DOY 143 through 152), the ice station drifted into slightly shallower water (~2500 m) on the continental slope. The background stratification was similar to segment 3. A large storm from DOY 143 to 145 significantly increased the northward ice drift speed.

A representative buoyancy frequency profile for each segment was calculated by averaging the CTD profiles from that segment (Figure 3). The weakening and shallowing of the seasonal pycnocline, as the ice station drifted northward and the season progressed into winter, can be seen by following the peak in N. The average profiles for segments 3 and 4 show no seasonal pycnocline. Major changes in the profiles between segments 1 and 2 and segment 3 and 4 are probably due to advection from the east, as documented by *Muench and Gordon* [1995].

Using $N(z)$, the energy parameter r was estimated independently from horizontal velocity (A2) and vertical

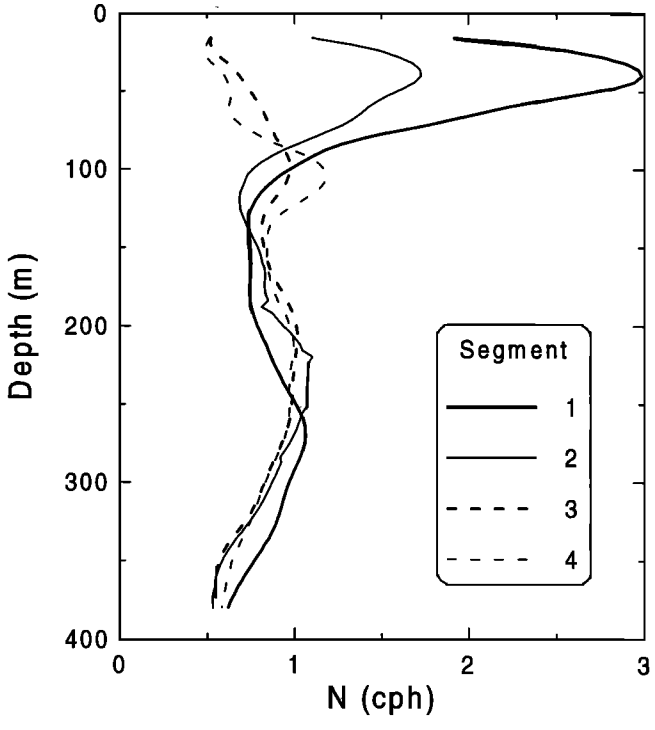

Figure 3. Average vertical profiles of buoyancy frequency for each segment, calculated from CTDs taken by Lamont-Doherty Earth Observatory and kindly provided by A. Gordon.

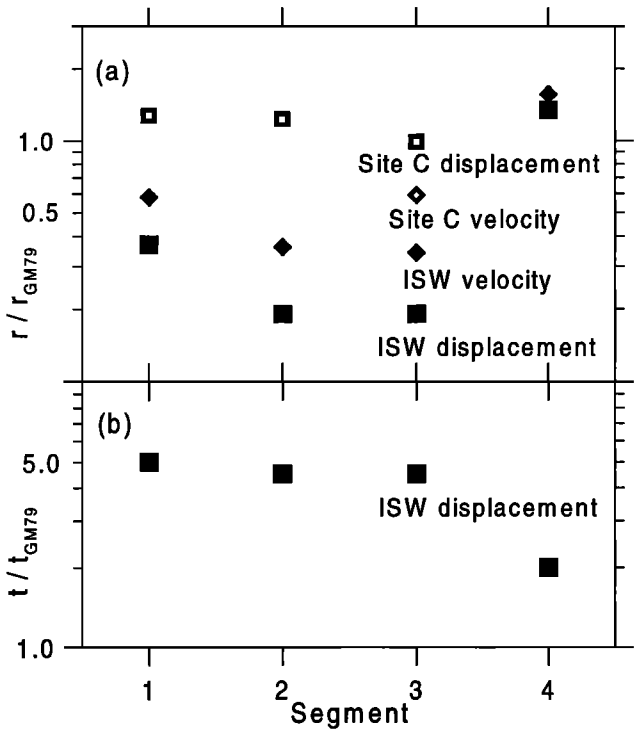

Figure 4. (a) Internal wave energy r/r_{GM79} as a function of segment, estimated from variances of vertical displacement (0.1 to 0.8 cph) at ISW (solid squares) and at site C (open squares) and horizontal velocity (0.15 to 0.35 cph) at ISW (solid diamonds) and site C (open diamonds). (b) Bandwidth t/t_{GM79} at ISW as a function of segment based on the vertical coherence of displacement.

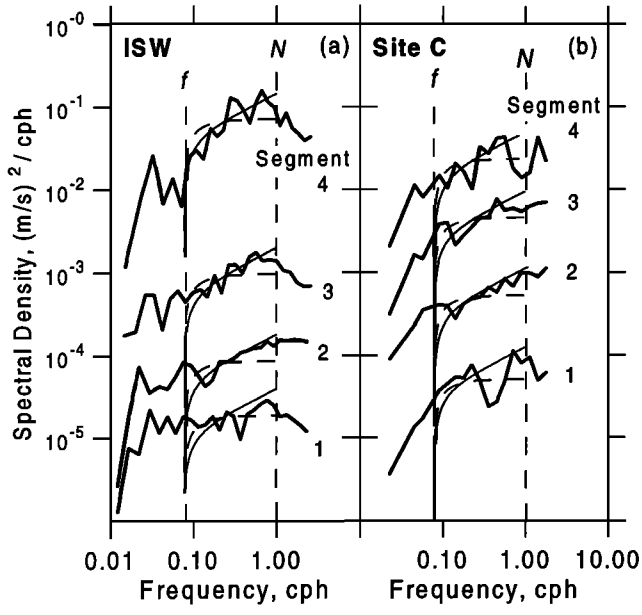

Figure 5. (a) Vertical velocity spectra for each segment calculated from the vertical displacement field at ISW at 250 m. Each successive segment is offset by an additional factor of 10. The GM79 spectrum (solid line) is plotted with the level adjusted to match the variance of the observed spectrum in each segment; a modified GM spectrum [*Levine et al.*, 1986] (dashed line) is also plotted where the displacement spectrum $\propto \omega^{-1.5}$ at high frequency. (b) Same as Figure 5a using data from site C at 200 m.

displacement (A1) as a function of time segment (Figure 4a). For comparison the estimates of r are scaled by r_{GM79}. The estimates of r from horizontal velocity and vertical displacement are within a factor of 2 of each other, demonstrating that the relationship between velocity and displacement is reasonably consistent with expectations from a field of internal waves. During segment 1, r was about half the GM level; in segments 2 and 3 the levels fell to a factor of 0.2 to 0.3. During segment 4 the variances increased to open ocean values as represented by the GM79 spectrum.

The individual frequency spectra that were used to calculate the variance in each segment are shown in Figures 5 and 6. To examine the spectral slope of the vertical displacement spectra, it is useful to convert to vertical velocity (w) spectra by multiplying by ω^2. The w spectrum was almost white in the internal wave band during segment 1. During later segments the spectral slope was nearly proportional to $\omega^{+0.5}$, which corre-

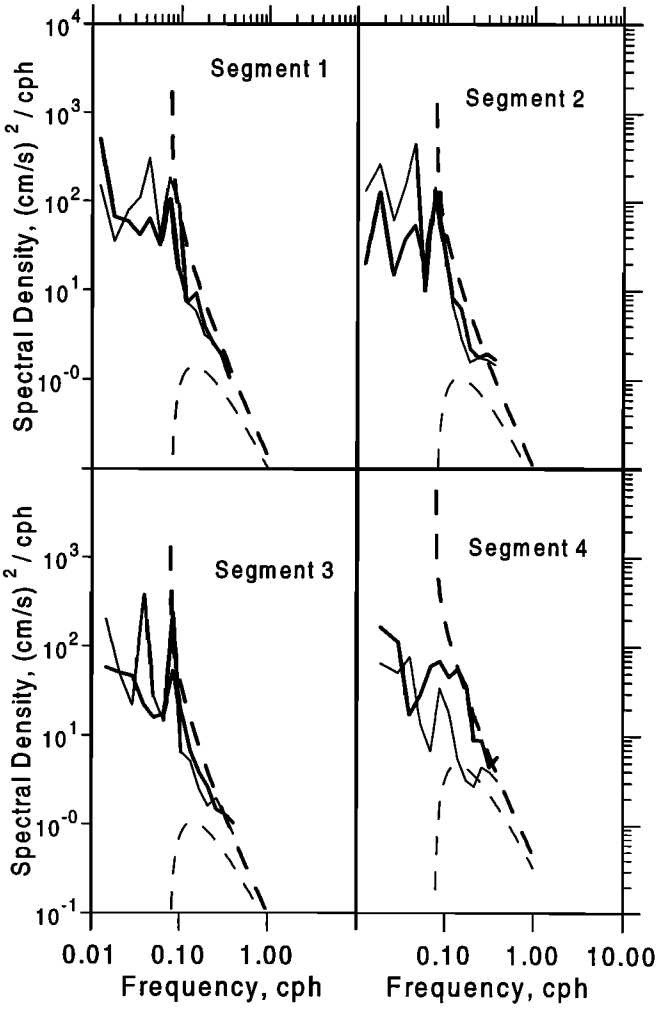

Figure 6. Horizontal velocity spectra for each segment at ISW at 200 m displayed in anticlockwise (bold solid curves) and clockwise (thin solid curves) components. The GM79 spectra for clockwise (bold dashed curves) and anticlockwise (thin dashed curves) components are plotted with the level adjusted to match the variance of the observed spectrum in each segment.

sponds to an $\omega^{-1.5}$ dependence in the vertical displacement spectrum. There was a distinct break in slope near N (about 1 cph) for the later segments. Only segment 4 hints at a low-frequency cutoff at f, the lower frequency bound for free internal waves. The shapes of the horizontal velocity spectra during segments 1, 2, and 3 are similar; the clockwise and anticlockwise components are indistinguishable from each other in the internal wave band (Figure 6). From theory, the ratio of the clockwise to anticlockwise components should decrease from near 1 at $\omega \sim N$ to 0 as $\omega \to f$. However only during segment 4 is the energy in the anticlockwise component higher than the clockwise, suggesting significant velocity fine structure during the first three segments. This is because velocity fine structure, which does not have a preferred polarization, would tend to produce spectra with equal rotary components. Since high frequencies were not resolved in the velocity spectra, a cutoff at N cannot be seen.

For comparison, the spectral shapes given by GM79 are also shown ((A1) and (A2)) (Figures 5 and 6). The spectral levels have been adjusted to match the observed values of r as shown in Figure 4a. Model curves for w spectra are also shown for a modified GM spectrum with an $\omega^{-1.5}$ vertical displacement dependence at high frequency ((A4) and (A5)) [*Levine et al.*, 1986]. After segment 1 the slope of the modified spectrum clearly fits the observations better. To avoid confusion, the modified GM spectrum is not shown for horizontal velocity (Figure 6) as the spectral slope at high frequency cannot be determined from the observations anyway.

The wave number bandwidth parameter t was estimated for each segment (Figure 4b) using the coherence of vertical displacement between vertically separated sensors (A9) (Figure 7). In the GM spectrum the vertical coherence is not a function of frequency. Although there is some frequency dependence in the data, values of t are chosen to give coherence levels (horizontal lines in Figure 7) that are in reasonable agreement with observations. The GM spectrum only applies to the frequency band between f and N. At the low-frequency end of the internal wave band near f, the coherence is undoubtedly influenced by the semidiurnal tide (section 3.2) and hence is not expected to follow the GM model. The high-frequency cutoff near N is clear during segments 3 and 4; however, the cutoff for other segments is less obvious. The vertical resolution of coherence is relatively coarse; the minimum vertical separation of temperature sensors in the permanent pycnocline was 30 m. During segment 4, when the coherence was highest, the dependence of the coherence on vertical separation reasonably follows the GM form (A9). During the other segments the coherence was significantly lower; coherence at separations greater than 30 m was often not significant and could not be fit to the GM level.

The wave number bandwidth t was typically larger than t_{GM79}, indicating that the observed wave field at ISW was less coherent than GM79 (Figure 4b). During segment 4, $t/t_{GM79} \approx 2$, while in the other segments, $t/t_{GM79} \approx 4$ to 5. However, the lack of a high-frequency cutoff in coherence during segment 2 casts doubt on using a pure internal wave model to interpret these observations: irreversible fine structure may be important in explaining the coherence structure.

The vertical wave number spectrum is another quantity that can be used to check the consistency of the spectral representation of the internal wave field. During each segment, wave number spectra were estimated from RSVP profiles (Figure 8). Spectra were calculated

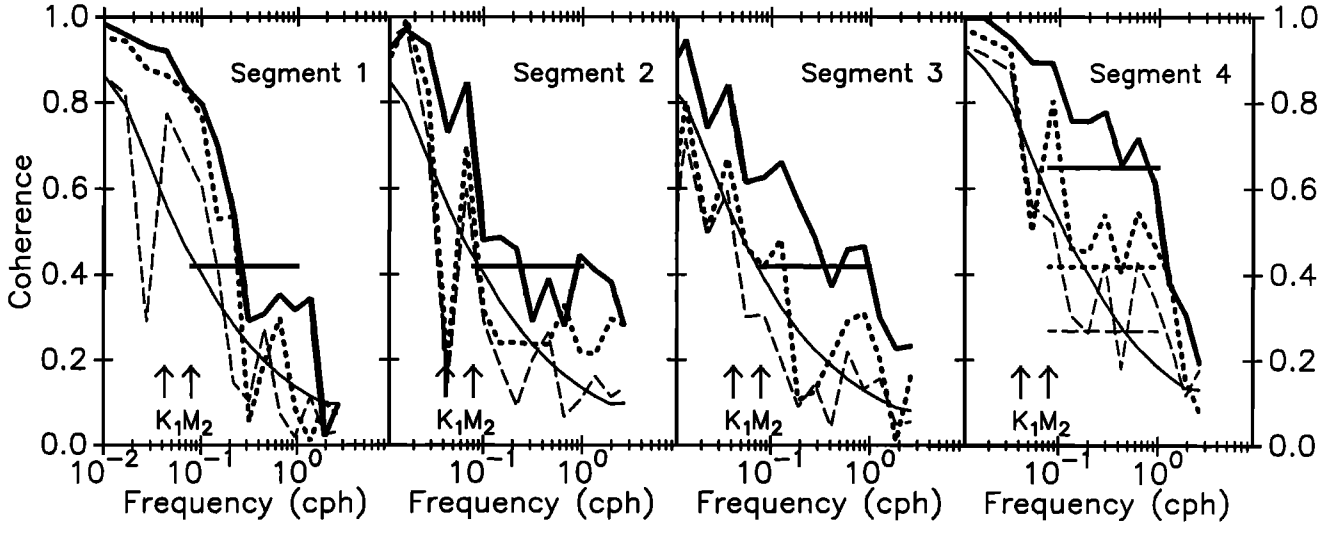

Figure 7. Coherence of vertical displacement at ISW as a function of frequency for vertical separations of 30 m (solid bold line), 60 m (dotted line), and 90 m (dashed line) for each segment. Values exceeding the thin solid line are nonzero at the 95% significance level. Horizontal lines indicating the coherence given by the GM79 spectrum (A9) for $t/t_{GM79} = 4$ (segments 1, 2, and 3) and $t/t_{GM79} = 2$ (segment 4) are also shown; horizontal lines are not shown for separations greater than 30 m for segments 1, 2, and 3.

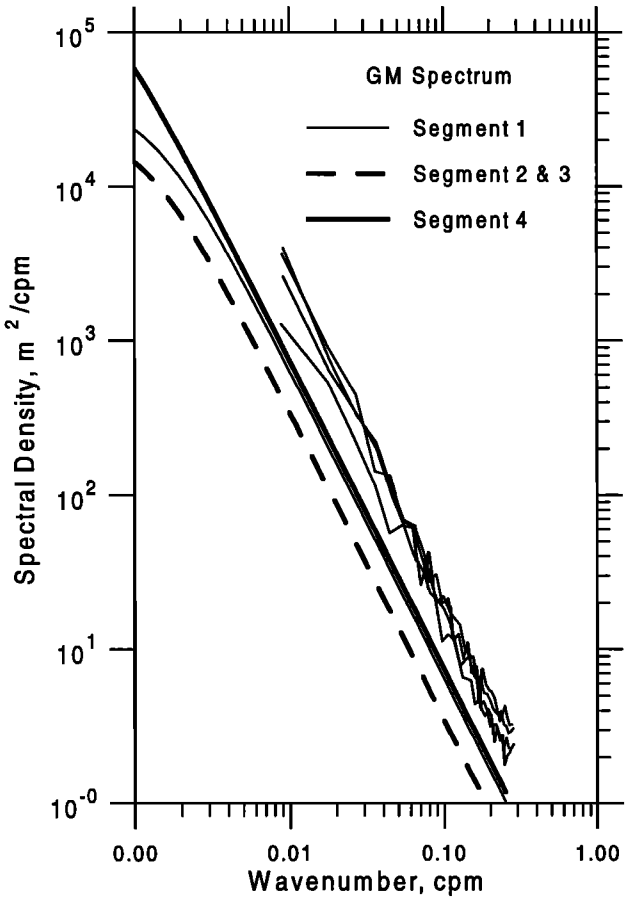

Figure 8. Vertical wave number displacement spectra at ISW for each segment. The spectra were estimated from vertical temperature profiles using an average vertical temperature gradient to convert to vertical displacement. As there is little difference among any of these spectra, no attempt has been made to label them individually. The GM79 spectra using estimates of r and t from each segment are also shown.

over a 256-m depth range centered at 250 m; larger vertical extent was not practical due to the vertical variability of the hydrography. The average vertical temperature gradient was used to convert temperature to vertical displacement. Overall, there is not a significant difference among the four spectra: all are within a factor of 2. For comparison, predicted GM wave number spectra are also plotted using values of r and t (A8) estimated from displacement and velocity spectra. The corresponding wave number spectra for the modified frequency spectrum ((A4) and (A5)) are not shown, as they have the same shape with the spectral level increased by a factor of 1.24 (A8). Over this range of vertical wave numbers the GM79 spectrum has a β^{-2} dependence and a spectral level that is approximately proportional to the product rt. The predicted GM spectra for the four segments are within a factor of 2 of each other as t tends to vary inversely with r. Specifically, in segments 1, 2, and 3, where the energy level r is lower than GM, the bandwidth t is higher. In segment 4, r is higher, but t is lower. Nonetheless the GM spectrum is lower than the observed spectrum by a factor of 2 to 4. This discrepancy might be due to the presence of irreversible temperature fine structure; it is possible for the fine structure to dominate the high wave number spectrum but not contaminate the frequency spectrum in the internal wave band (see section 4).

3.1.3. Observations at site C. The characterization of the internal wave field is less certain at site C as fewer internal wave observations were made. The time series of vertical displacement and horizontal velocity variance at 200 m are plotted for the same frequency bands as the ISW data (Figure 2). The displacement variance was generally higher at site C than at ISW, and the variability between the two sites was not correlated. Although the velocity variance at site C could only be estimated over the latter portion of the record, it is somewhat correlated with the displacement variances.

Estimates of r for each of the time segments are given in Figure 4. In contrast to ISW the spectral levels of displacement were near GM levels for the first three segments; an estimate for segment 4 was not possible due to the lack of reliable observations. The velocity variance for segment 3 is also within a factor of 2 of the GM level.

The w spectra from site C for each segment are shown in Figure 5b along with the modeled spectra. As found at ISW the spectra are closer to the modified GM spectral shape, especially during segments 2 and 3. Unfortunately, coherences and wave number spectra are not available from site C, preventing a more detailed comparison. Possible reasons for the difference in the amplitude of the wave field between the two sites are discussed in section 4.

3.2. Tides

Tides and related processes can strongly influence the hydrography, mean circulation, and water mass modification processes in ice-covered seas [*Foster et al.*, 1987; *Padman et al.*, 1992; *Padman*, 1995]. In the Weddell Sea, tidal currents have been implicated in the development and maintenance of low ice concentrations and thus more rapid ice production at the Filchner and Ronne Ice Fronts [*Foldvik and Gammelsrød*, 1988]. The formation of Weddell Sea Deep and Bottom Water by mixing of cold and highly saline shelf water types with Warm Deep Water at the shelf/slope front is also enhanced by tide-generated mixing [*Foster et al.*, 1987]. Models of barotropic tides in the Weddell Sea [e.g., *Genco et al.*, 1994; *Robertson et al.*, 1996] suggest that barotropic tidal currents over some regions of the shelves and upper slope of the southwestern Weddell Sea can exceed 0.5 m s^{-1}. Since this velocity greatly exceeds the mean currents of less than 0.1 m s^{-1} associated with the Weddell Gyre, tides also increase the benthic mixing rate and the effective drag felt by the mean circulation. A separate study extending the preliminary model results described by *Robertson et al.* [1996]

is presently being conducted to better understand the various roles that tides play in the large-scale oceanography of the Weddell Sea. The present paper concentrates only on tidal currents measured with current meters deployed at ISW and the associated remote camps.

Barotropic diurnal and semidiurnal tidal components are generated at precise frequencies with currents that are typically quite uniform vertically. Surface displacements are usually less than 1 m in deep water, although large vertical displacements of subsurface isopycnals are possible where strong barotropic tidal currents flow across steep bottom slopes [*Padman et al.*, 1992]. The diurnal frequency band may also contain an internal (baroclinic) response, but at the latitude of the Weddell Sea (~60°–80°S), diurnal internal waves cannot exist as free waves and are probably not significant. In contrast, the semidiurnal frequency band may include a freely propagating internal tide: with a period of about 12.42 hours the M_2 tide has a critical latitude (θ_c) of 75°2.8′. This latitude is south of the present study area but within the Weddell Sea. *Nøst* [1994] has investigated the modification of the vertical structure of M_2 horizontal barotropic currents near θ_c in the Barents Sea in the eastern Arctic Ocean, finding increasing shear and a thicker benthic boundary layer there. Similar modification is expected near θ_c on the southern Weddell Sea shelf.

Table 1. Tidal Analysis of Current Meter Data for Time Segments 1 (DOY 80–100), 2 (DOY 101–120), and 3 (DOY 121–143) for ISW and Remote Sites C, D, and E (see Figure 1)

	E	*C*	ISW	*D*
		O_1 / *Period 1*		
Major	2.34	1.58	1.05	1.44
Minor	1.4	0.98	−0.44	−0.34
Inclination	106	174	10	48
Phase (G)	122	173	9	12
		O_1 / *Period 2*		
Major	N/A	N/A	1.68	N/A
Minor	N/A	N/A	−1.2	N/A
Inclination	N/A	N/A	35	N/A
Phase (G)	N/A	N/A	114	N/A
		O_1 / *Period 3*		
Major	3.73	2.45	1.64	N/A
Minor	0.49	−0.76	−1.25	N/A
Inclination	2.2	4	166	N/A
Phase (G)	257	249	52	N/A
		M_2 / *Period 1*		
Major	4.14	2.99	2.08	1.81
Minor	−0.24	−0.71	−1.35	−1.38
Inclination	176	13	32	41
Phase (G)	52	208	182	180
		M_2 / *Period 2*		
Major	5.8	2.08	2.05	N/A
Minor	0.44	0.51	−1.05	N/A
Inclination	174	154	154	N/A
Phase (G)	111	85	125	N/A
		M_2 / *Period 3*		
Major	4.58	2.39	2.6	N/A
Minor	0.43	−0.82	−0.97	N/A
Inclination	166	5	175	N/A
Phase (G)	103	261	84	N/A

The vertical displacement of the pycnocline due to the semidiurnal baroclinic tide in the open ocean can be quite large, typically ~10 m. Significant vertical structure in both the current and vertical displacement fields is also common. The internal tide tends to vary in time and therefore occupies a broader frequency band than the barotropic tide. This variability is probably due to variations in the background velocity and density fields through which the wave has propagated. Distinguishing between barotropic and internal tidal components can be difficult, especially from observations such as those obtained during ISW from moving moorings with poor vertical resolution (current meters only at 50- and 200-m depth). However, some basic features of the tidal signals can be explored with these data.

Tidal analyses were performed on the time series of currents at each drift station shown in Figure 1, using a simultaneous least squares fit of the principal tidal constituents [*Foreman*, 1978]. Constituents were determined for time segments 1, 2, and 3. Each of these segments is sufficiently long to separate the two principal semidiurnal (M_2 and S_2) and two diurnal (O_1 and K_1) constituents. The properties of the tidal ellipses for these four constituents are shown in Table 1 for each segment and site. Since absolute currents were determined by removing the ice motion from the measured ice-relative velocities, errors in the estimated ice motion will contaminate estimates of absolute current. Although it cannot be verified independently, we believe that these errors are small relative to most estimated tidal signals [*Muench and Gordon*, 1995].

There was little difference between the tidal ellipse properties at 50 and 200 m at ISW and other sites when data at both depths were available. We therefore infer that the baroclinic tide was weak in both the diurnal and semidiurnal bands. Not only were the currents at 50 and 200 m nearly the same, but peaks in vertical displacement spectra, which would indicate baroclinic tides, are not apparent (Figure 5). The steadiness of the observed ellipses also suggests that the currents were dominated by the barotropic tide, since measurements from other regions indicate that tidal ellipse properties in the presence of energetic internal tides are typically highly variable.

We have recently developed a high-resolution barotropic tidal model of the Weddell and Scotia Seas [*Robertson et al.*, 1996]. This model is forced by boundary con-

Table 1. (continued)

	E	*C*	ISW	*D*
		K_1 / Period 1		
Major	3.38	2.49	1.68	3.18
Minor	−0.58	−0.68	−0.99	−1.5
Inclination	160	177	31	79
Phase (G)	341	343	157	79
		K_1 / Period 2		
Major	3.83	3.53	2.18	N/A
Minor	0.14	−1.49	−1.1	N/A
Inclination	169	5	22	N/A
Phase (G)	342	199	130	N/A
		K_1 / Period 3		
Major	2.23	1.57	1.18	N/A
Minor	0.32	−0.23	−0.94	N/A
Inclination	13	17	173	N/A
Phase (G)	158	122	297	N/A
		S_2 /Period 1		
Major	4.14	2.09	1.33	4.06
Minor	0.27	−0.39	−0.83	0.82
Inclination	140	20	61	114
Phase (G)	49	142	121	57
		S_2 /Period 2		
Major	N/A	N/A	1.47	N/A
Minor	N/A	N/A	−0.77	N/A
Inclination	N/A	N/A	44	N/A
Phase (G)	N/A	N/A	59	N/A
		S_2 /Period 3		
Major	2.09	1.97	1.38	N/A
Minor	−0.02	0.11	−0.31	N/A
Inclination	105	27	59	N/A
Phase (G)	249	320	287	N/A

Major and minor axes are in cm s^{-1}: negative minor axes implies that the current ellipse rotates clockwise; otherwise rotation is anticlockwise. Inclination is taken anticlockwise from east.

ditions obtained from an inverse model of global oceanic tides [*Egbert et al.*, 1994], which uses the Laplace tidal equations, and data from tide gauges and the TOPEX satellite altimeter. Modeled tidal currents are sensitive to the bathymetry, which is poorly known in this region [*LaBrecque and Ghidella*, 1993]. Furthermore, there are no tide gauge or altimeter data in the southern and western Weddell Sea; therefore tidal predictions are primarily extrapolated by the model physics from the data-constrained Southern Ocean region to the north. Considering these caveats, however, the modeled major-axis current amplitudes are compared with observations in Figure 9, for an east-west transect along 67.5°S during time segment 3. The model predicts that the K_1 tidal current will reach a maximum amplitude of 0.05 m s^{-1} near the continental shelf break. Larger model amplitudes are found at other latitudes, notably over the submarine ridge near 68.5°S (see Figure 1). Measured major axis K_1 amplitudes are slightly higher than predicted values, which may be due to actual bathymetry differing from values used in the model. The modeled cross-slope diurnal variability is reminiscent of the structure of diurnal shelf waves found from mooring measurements in the southern Weddell Sea by *Middleton et al.* [1987] and the analytical model of *Saint-Guily* [1976] for topographically trapped barotropic shelf waves next to a wide, flat continental shelf.

Semidiurnal (M_2) currents in the model are consistent with the observations, although the measurements are all east of the predicted peak of the M_2 current (0.15 m s^{-1}) over the outer shelf, near the mean location of the shelf/slope front [*Muench and Gordon*, 1995]. As with the K_1 tidal constituent, higher values of up to 0.35 m s^{-1} are found over the ridge near 68.5°S. The peak model currents are substantially higher than the mean along-slope barotropic circulation of 0.08–0.1 ms^{-1} at the front. *Muench and Gordon* [1995] observed a dense plume of extremely cold and saline water flowing down the continental slope in the ISW region. This water presumably originates in the southern Weddell Sea as

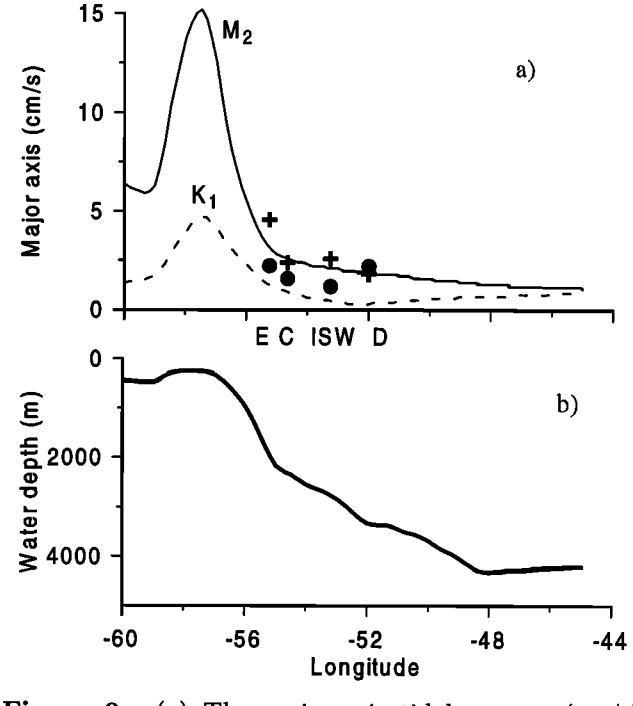

Figure 9. (a) The major-axis tidal current (cm/s) for M_2 (solid line) and K_1 (dashed line) at latitude 67.5°S as a function of longitude, from the tidal model of *Robertson et al.* [1996]. Observed tidal current for M_2 (plusses) and K_1 (circles) at ISW and remote sites C, D, and E. (b) Water depth along the same transect as in Figure 9a.

a plume of modified Ice Shelf Water flowing out of the Filchner Depression [*Gordon et al.,* 1993b]. The degree to which this plume mixes with the ambient Warm Deep Water and Weddell Sea Deep Water during its passage down the slope determines the properties of the resultant Weddell Sea Bottom Water. The mixing rate will be in part determined by benthic stirring and shear at the interface between the dense plume and the overlying fluid. Enhanced mixing processes might be caused by benthic tidal currents, as well as baroclinic tides and higher-frequency internal gravity waves that can both be excited by the interaction of tidal flows with the shelf/slope topography.

4. Discussion

We next consider the effect of the internal wave continuum on regional hydrography and circulation. The parameters that characterize the observed internal wave continuum from ISW and site C are summarized in Table 2 along with the same parameters derived from other experiments where both internal wave energy and bandwidth were estimated. The observations from the Arctic Internal Wave Experiment (AIWEX) and the Coordinated Eastern Arctic Experiment (CEAREX) were both made at high latitudes under pack ice in the northern hemisphere. The Internal Wave Experiment (IWEX) in the Atlantic Ocean and the Mid-ocean Acoustic Transmission Experiment (MATE) in the Pacific Ocean were experiments designed especially to resolve the internal wave field in the open ocean. The GM formulation can also be considered as representative of open ocean internal wave data, since the energy levels and bandwidth parameters were determined empirically from a synthesis of field observations.

The presence of pack ice may alter the internal wave continuum from that observed in an ice-free ocean. It has been suggested that the wave field below the pack ice is lower than the GM level because of a reduction in sources of internal waves [*Levine et al.*, 1985] or an increase in wave dissipation [*Morison et al.*, 1985]. However, the identity of the wave sources that are the most important remains uncertain. In ice-free oceans, wind stress is certainly important in generating near-inertial waves and may directly generate a significant amount of internal waves in the continuum band as well [*Rubenstein*, 1994]. The energy pathway from wind stress to the wave field is certainly modified, if not reduced, by the ice. For example, the horizontal scale of the surface stress is probably greater under compact sea ice than in the open ocean. Generation mechanisms involving surface waves are not significant in an ice-covered ocean.

Observations suggest internal wave energy away from significant topography is lower under pack ice [*Levine et al.*, 1985]. Continuum energy levels at ISW were lower than GM79 for most of the experiment (segments 1, 2, and 3). The under-ice wave field in the Beaufort Sea (AIWEX) was exceptionally low in energy, 0.03 to 0.07 of the GM level [*Levine et al.*, 1987]. On the other side of the Arctic Ocean in the Nansen Basin, low levels near 0.33 GM were also observed [*Plueddemann*, 1992]. Near topography, energy seems to increase even in ice-covered seas. This was dramatically demonstrated in observations from the Arctic Environmental Drifting Buoy (AEDB) [*Plueddemann*, 1992] that showed an increase from the low energy in the Nansen Basin to GM levels when crossing the Yermak Plateau. In the same region during CEAREX a similar increase in energy, a factor of 0.5 to 3 times GM, was found as the ice camp drifted from the deep water onto the central slope of the plateau [*Wijesekera et al.*, 1993; *Padman and Dillon*, 1991]. This was somewhat surprising since the plateau is a fairly deep feature, reaching only to 600 m from the sea surface. However, the high internal wave energy is thought to be related to the barotropic diurnal tidal current that is amplified by interaction with the plateau [*Padman et al.*, 1992]. The difference in the internal wave field between ISW and site C during segments 1, 2, and 3 appears to be analogous to the Arctic observations: energy levels tend to be lower than GM over deep water, and levels are near or above GM close to topographic features where the barotropic tide is larger. While there appears to be a correlation between energy of the barotropic tide and that of the internal wave continuum, a dynamic link has not been established.

During segment 4 the internal wave energy at ISW increased to near GM levels. This increase coincided with an increase in ice drift speed due to a storm. To demonstrate that the increase was due to internal waves and not the effects of mooring motion, the spectrum of pressure that directly measures vertical mooring motion was compared with the displacement spectrum inferred from temperature (not shown). The pressure spectrum was a factor of 10 to 100 lower than the displacement spectrum; that is, even though the vertical motion of the mooring increased during the storm, it was significantly less than the measured displacements at internal wave frequencies. The correlation of increased wave energy with faster ice drift suggests that wave energy may be input by the stress at the ice/water interface. The mechanism by which the waves would be generated is, however, uncertain. *McPhee and Kantha* [1989] described a mechanism by which form drag over ice keels could generate internal waves in the underlying pycnocline. In the western Weddell Sea however, after the decay of the seasonal pycnocline, the mixed layer is so deep that flow relative to typical ice keels resulting from rafting and deformation is not likely to be an efficient generator of internal waves. Several icebergs in the vicinity of the camp may have had sufficient draft to interact with the permanent pycnocline. However, more study is needed to assess the possibility that icebergs contribute significantly to internal wave production in this region. It is also possible that the increase in internal wave energy is simply related to the drift of the ice camp into a region of higher mean energy,

Table 2. Estimates of Internal Wave Energy r and Bandwidth t for ISW and Prior Observations

Experiment	Location/ Reference	Energy r/r_{GM79}	Bandwidth t/t_{GM79}	N, $10^{-3}s^{-1}$	f, $10^{-4}s^{-1}$	ω Slope	ϵ_{HWF}, $10^{-9}W\,kg^{-1}$ (equation (4))	K_d, $10^{-6}m^2s^{-1}$ (equation (5))
GM79	[*Munk*, 1981]	1	1	5.24*	1*	−2	0.42*	3.1*
ISW	western Weddell Sea							
Segment 1	(this paper)	0.4–0.6	5	1.6–1.9	1.4	−1.5	...	...
Segments 2 and 3		0.2–0.4	4–5	1.6–1.9	1.4	to	0.021–0.38	1.8–21
Segment 4		1.3–1.6	2	1.6–1.9	1.4	−2	0.023–0.05	19–30
Site C								
Segments 1, 2, and 3		1.0–1.3	...	1.0–1.1	1.4		...	...
IWEX	NW Atlantic [*Müller et al.*, 1978]	0.25	0.9–1.6	0.63–4.7	0.68		0.00013–0.036	0.064–0.33
MATE	NE Pacific [*Levine et al.*, 1986]	0.9	2	1.7–2.3	1.0	−1.7	0.1–0.2	7.4–8.0
AIWEX	western Arctic Ocean [*Levine et al.*, 1987; *Levine*, 1990]	0.03–0.07	10	8.7	1.4	−1.2	0.1–0.8	0.4–2.1
CEAREX	eastern Arctic Ocean							
Period 1	[*Wijesekera et al.*,	0.26–0.3	1–2	2.8–6.8	1.4		0.01–0.35	0.23–1.5
Period 2	1993]	0.6–1.3	2–3.3	2.8–6.8	1.4		0.93–3.9	6.0–65
Period 3		1.6–2.3	1–1.3	2.8–6.8	1.4		0.73–5.0	9.8–32

Values are given realtive to GM79 levels. Estimates of ϵ_{HWF} (equation (4)) and K_d (equation (5)) are also given.
* For GM79, values of ϵ_{HWF} and K_d were calculated using typical midlatitude values of f and N.

perhaps closer to a source of bottom-generated waves. Other measurements would be required to distinguish between local generation and spatial variability.

Observed vertical displacement spectra indicate that the spectral slope at high frequency ($\omega \gg f$) was closer to -1.5 during most time segments than the -2 slope of GM79. A slope somewhat less steep than -2 is a common feature observed in the open ocean as well [e.g., *Levine et al.*, 1983; *Briscoe*, 1975]. However, these spectra are far from the spectral slope of about -1.1 that was found in the Beaufort Sea (AIWEX) and Nansen Basin (AEDB).

Climatological variability of wave number bandwidth is hard to quantify because there are few studies with which to compare. At ISW during segments 2 and 3 the bandwidth was significantly higher than typical open ocean values. In segment 4 the bandwidth decreased as the energy level increased. The inverse relationship between energy and bandwidth, or equivalently the constancy of the product rt, is suggested to hold for the historical data in Table 2 (Figure 10). However, more data are needed to establish a significant correlation. The product rt also appears in the expression for the reciprocal Richardson number function (Ri^{-1}) defined by *Munk* [1981] to be σ_s^2/N^2 , where σ_s^2 is the variance of the vertical shear due to internal waves. Using the GM spectrum, it can be shown that

$$Ri^{-1} \propto rt\beta_c \tag{3}$$

where β_c is the high vertical-wave number cutoff. It has been suggested [*Munk*, 1981] that the wave field seeks to maintain a constant Ri^{-1}. If β_c is constant, there would be a tendency for rt to be constant.

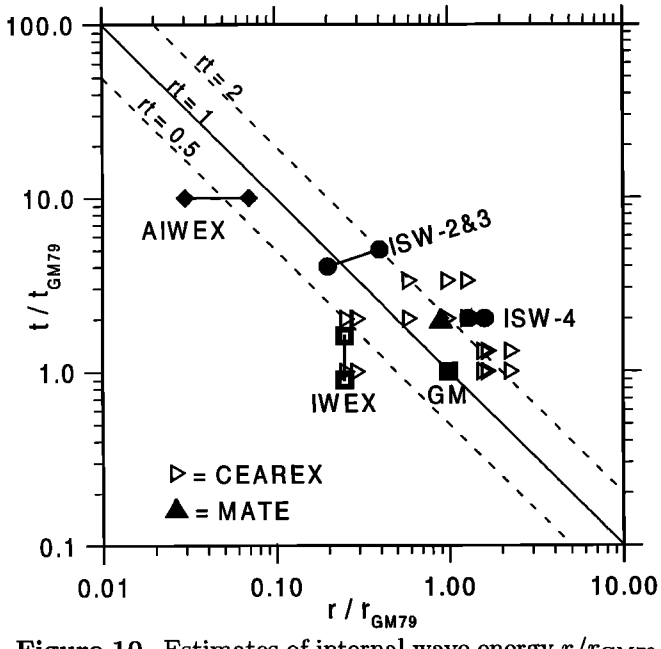

Figure 10. Estimates of internal wave energy r/r_{GM79} and bandwidth t/t_{GM79} for each time segment (ISW). Estimates from other observations given in Table 2 are also shown.

Overall, the observations at ISW are most consistent with internal waves during the high-energy segment 4. Not only is the energy near GM79 levels at this time, but the frequency spectrum of w shows the clearest cutoffs near both f and N. The coherence structure also follows the model dependence more closely than during other segments and has a sharp cutoff at N. The preference for anticlockwise current in the rotary spectrum follows more closely the theoretical prediction than at other times (Figure 6).

Vertical wave number spectra of displacement sometimes show a break in slope, usually near 0.1 cpm, indicating a high wave number cutoff [*Gregg*, 1977]. At ISW the temperature vertical wave number spectra have a β^{-2} dependence with no hint of a break or cutoff (Figure 8). There was also no significant difference among the spectra from the time segments. The spectra are about a factor of 2 to 4 higher than predicted by the GM formulation using the estimated values of r and t. Differences from the GM spectrum may be due to the presence of temperature fine structure. The presence of fine structure does not, however, invalidate the interpretation of the w frequency spectrum as internal waves. The model developed by *Levine and Irish* [1981] shows that when this high-wave number fine structure is advected by the internal wave field, the corresponding temporal signal usually occurs at frequencies above N. With the magnitude of fine structure present in the wave number spectra, it is likely that the estimated displacement frequency spectra are dominated by internal waves in the frequency band f to N.

The wave number spectra at ISW are consistent with those found in 1976 by *Middleton and Foster* [1980] in a region just north of the northernmost extent of ISW (65°S, 51°W). Using a series of 25 CTD casts from a ship locked in the pack ice, vertical wave number temperature spectra were estimated over the depth range 89–345 m. These spectra also exhibited a -2 spectral slope with no high-wave number cutoff. The observed spectral level was higher than GM79 (a factor of 3 or 4) and was believed to be due to fine structure caused by intrusions.

One major justification for this study of internal waves in the western Weddell Sea was to assess their role in determining the upward heat flux from the Warm Deep Water (WDW) toward the surface by turbulent mixing. In other locations, internal waves undoubtedly play a role in mixing the ocean; however, several studies now suggest that "typical" mixing rates are too low to provide the necessary fluxes through the permanent pycnocline [*Gregg*, 1989; *Ledwell et al.*, 1993]. Some have suggested that the effective diapycnal fluxes in mid-ocean are a result of intense, localized mixing, probably around the basin perimeters, followed by isopycnal spreading into the ocean interior [e.g., *Welander*, 1959; *Armi*, 1978; *Ivey*, 1987]. In the Arctic Ocean, there is evidence that diffusivities increase by 2–3 orders of magnitude from the deep basins to near the Yermak

Plateau [*D'Asaro and Morison*, 1992; *Padman*, 1995]. A similar spatial variation is likely in regions such as the western Weddell Sea, where benthic generation of internal waves due to spatially variable tidal currents may be a significant source of internal wave energy.

To better understand the link between internal waves and turbulent mixing, *Gregg* [1989] explored the relationship between the internal wave field and the dissipation of turbulent kinetic energy. Expressions were derived based on the weak-interaction theory of *McComas and Müller* [1981] (hereafter MM) and the strong interaction model of *Henyey et al.* [1986] (hereafter HWF):

$$\epsilon_{\mathrm{HWF}} = \frac{1.67}{\pi^3}\cosh^{-1}\left(\frac{N}{f}\right)N^2 f r^2 t^2$$
$$\epsilon_{\mathrm{MM}} = \left(\frac{27\pi}{32\sqrt{10}}+1\right)N^2 f r^2 t^2, \quad (4)$$

where the energy and bandwidth parameters r and t have been used to replace the four GM parameters. This substitution clarifies the wave field parameterization in these models of ϵ. Both of these expressions depend upon the product rt; however, ϵ_{MM} is a factor 7 to 10 larger than ϵ_{HWF}. For typical ocean values of f and $N, \epsilon \propto N^2$ in both formulations. (Note that ϵ_{HWF} is based on GM79 [*Munk*, 1981]; *Gregg and Kunze* [1991] suggest that the shear is better represented by GM76 which increases ϵ_{HWF} by a factor of approximately 2 [*Wijesekera et al.*, 1993; *Polzin et al.*, 1995].) Using observations of r, *Gregg* [1989] found good agreement with the HWF formulation. From estimates of r and t, *Wijesekera et al.* [1993] found during CEAREX that ϵ was near ϵ_{HWF} in regions where the wave field is consistent with the GM model and near ϵ_{MM} in higher-energy regions. Estimates of ϵ_{MM} and ϵ_{HWF} were made for ISW and the other wave fields described in Table 2. Direct measurements of ϵ at ISW at 250-m depth were typically limited by the instrument's noise floor, which was near 2×10^{-9} m^2 s^{-3} [*Robertson et al.*, 1995]. Values of ϵ_{HWF} are less than the noise floor estimates and therefore are not inconsistent with the direct measurements. Estimates of ϵ_{MM} are larger than the observations, especially during segment 4.

The diapycnal eddy diffusivity K_d can be estimated from ϵ (Table 2) by assuming [Osborn, 1980]:

$$K_d \approx \frac{\Gamma\epsilon}{N^2}, \quad (5)$$

where Γ is the mixing efficiency, defined as the ratio of buoyancy flux to the dissipation rate of turbulent kinetic energy. A canonical value of Γ is 0.2, although estimates range from about 0.05 in the midlatitude permanent thermocline to about 0.7 near energetic tidal fronts in coastal waters [*Gargett and Moum*, 1995]. Using $\Gamma = 0.2$ and the observed vertical temperature gradient, a heat flux of about 1 W m^{-2} is estimated from ϵ_{HWF}; a value closer to 7 W m^{-2} is obtained using ϵ_{MM}. However, as discussed above, we believe that the wave field characteristics at ISW are more consistent with the HWF model, and hence we favor the lower estimate (1 W m^{-2}) obtained from HWF. This value is also consistent with measurements of mean upward heat flux of 1–2 W m^{-2} through the boundary layer directly beneath the sea ice [*McPhee and Martinson*, 1994; *Robertson et al.*, 1995], although it is less than the mean ocean/ice heat transfer of 7 ± 2 W m^{-2} determined from the thermodynamic balance of the sea ice [*Lytle and Ackley*, 1996] during the same program. In either case, the mean upward flux at ISW is less than the area-averaged value required to explain the observed heat loss from the WDW in the Weddell Gyre [*Fahrbach et al.*, 1994]. Other processes might be involved in the loss of heat from the WDW in this region; for example, *Robertson et al.* [1995] noted that an additional (but unknown) flux could be associated with intrusions indicative of mixing along isopycnals that slope upward to both the east and west of ISW. We conclude that mixing due to internal waves along the ISW drift track is not significant relative to other heat loss mechanisms within the gyre. However, site C observations indicate that internal wave increases to the west of ISW, possibly associated with increased tidal energy further up the continental slope (Figure 9). Pycnocline mixing due to these internal waves might therefore drive upward diapycnal heat fluxes that could be important to the mean loss of WDW heat in the gyre. Strong mixing near the shelf break would be particularly significant since it is the region of the shelf/slope front, where the high-salinity shelf waters mix with WDW to form Weddell Sea Deep and Bottom Water, which ultimately contribute to the production of Antarctic Bottom Water.

If the product rt were truly constant, the implication for the parameterizations of ϵ (4) would be profound: dissipation would be only a function of N and f, and eddy diffusivity (5) would be a function of only Γ and f. Although Figure 10 suggests that rt might be approximately constant, K_d is proportional to $(rt)^2$ ((4) and (5)) and hence is relatively sensitive to small errors in estimating r and t. It is especially difficult to characterize the internal wave bandwidth by a single constant parameter t, requiring many assumptions about the form of the spectrum. It therefore remains an open question as to whether it is reasonable to estimate ϵ from easily measured average properties of the internal wave field. One way to address this question is to make more concurrent direct measurements of dissipation and the internal wave spectrum. Observations in regions where the wave spectrum deviates significantly from the Garrett-Munk description could be most enlightening. Direct numerical simulation is another tool that might contribute to our understanding of the link between internal waves and dissipation.

5. Summary

The internal wave field and tidal currents have been measured for the first time in the perennially ice-covered western Weddell Sea. The observations were made dur-

ing a joint U.S./Russian experiment from the drifting Ice Station Weddell 1 (ISW) and at nearby sites C, D, and E (Figure 1). Time series of temperature and water velocity were made from moorings attached to the ice during a 4-month period in early 1992 as the camp drifted 600 km northward. About 700 vertical profiles resolving microscale temperature and velocity shear were also obtained. The present analysis has focused on observations in the upper permanent pycnocline at 200- to 300-m depth.

To study the internal wave continuum, the time series at ISW and site C were divided into four segments, defined to capture the major variations in background stratification and bottom topography (Figure 3). The measurements were compared with the Garrett-Munk spectrum, which is used as a representative description of open-ocean internal waves. We follow *Desaubies* [1976] and express GM79 as a function of two independent parameters: energy level r and wave number bandwidth t. At ISW and site C, estimates of r were made for each segment (Figure 4 and Table 2) by comparing observations with the GM79 spectrum (Figures 2, 5, and 6). At ISW the bandwidth t was estimated from vertical coherences (Figures 4 and 7); bandwidth estimates could not be made at site C. The internal wave field was found to have lower energy than GM79 by a factor of 0.2 to 0.6 at ISW during segments 1, 2, and 3 and energy near GM79 during segment 4; energy near GM79 at site C for segments 1, 2, and 3; and lower coherence than GM79 at ISW. The bandwidth was a factor 2 higher during segment 4 and a factor of 4 to 5 higher in the other segments.

Overall, at ISW the observations were most consistent with internal waves being the dominant source of variability during the highest-energy segment 4. The energy increase might have been related to the increase in the speed of the pack ice due to a storm or may indicate horizontal variability in the energy of the wave field. Spatial gradients of the internal wave variance and coherence structure could be due to variations in the dynamics caused by differences in water depth, barotropic tidal current, and proximity of topography. During this segment the frequency cutoffs in vertical velocity spectra at f and N are more distinct (Figure 5), the anticlockwise component of the rotary spectrum dominates as expected (Figure 6), and the coherence structure most closely follows the GM79 formulation (Figure 7). During the other segments, some of these aspects of the wave field do not fit the GM79 model as well as in segment 4.

At site C, there was also significant variability in internal wave variance (Figure 2), although the segment averages were near GM levels (Figure 4). Higher spectral levels at site C than ISW may be due to the horizontal variation of the internal wave variance.

The ISW wave field is put into a broader context by comparing the results from other experiments where both r and t were estimated (Figure 10 and Table 2). A common feature with observations in other ice-covered oceans is the significant time variability of the wave field. The historical data indicate that the product rt remains within a factor of 2 of the GM79 value (Figure 10). However, more observations are needed to determine if this relationship between r and t is robust.

On the basis of the estimates of internal wave parameters, the dissipation of turbulent kinetic energy ϵ was calculated from the models of HWF and MM as presented by *Gregg* [1989] (Table 2). The model predictions of ϵ in the permanent pycnocline could not be confirmed directly by measurement as the modeled ϵ was well below the instrumental noise level of 2×10^{-9} m^2 s^{-3}. Model values ϵ_{HWF} were a factor of 2 to 10 below the noise floor and hence not inconsistent with the direct measurements. While model estimates of ϵ_{MM} are closer to the instrumental noise level, our understanding of the intermittency of ϵ, combined with similar observations made in the Arctic during CEAREX [*Wijesekera et al.*, 1993], leads us to believe that the HWF model is more appropriate for the present data. In this case, an upward heat flux of approximately 1 W m^{-2} is implied, which is significantly less than the basin-averaged value of about 20 W m^{-2} that has been inferred from the heat budget of WDW in the Weddell Gyre [*Fahrbach et al.*, 1994]. From this and a related study [*Robertson et al.*, 1995] we conclude that most mixing of WDW must occur either to the east of ISW, where the ice cover varies seasonally, or farther west on the upper continental slope and shelf (e.g., site C), where internal wave activity appears to be higher.

The current in both the diurnal and semidiurnal frequency band appears to be dominated by the barotropic tide. The horizontal velocity decomposed into tidal ellipses as a function of time and space is nearly the same at 50 and 200 m, as expected for a barotropic process. A large vertical displacement signal is often an indicator of internal tide; however, none of the observed vertical displacement spectra have peaks at tidal frequencies. Since the near-inertial and semidiurnal frequency bands are very close, confusion in interpreting the source of the observed signal between tidally forced motion and surface-forced near-inertial oscillations is possible. However, near-inertial motion appears to be quite small, based on the lack of response to storm events even at 50-m depth, and given that the expected anticlockwise component does not dominate. A regional, high-resolution barotropic tidal model predicts an increase in current amplitude toward shallow water, in agreement with the observations.

Appendix

The spectral relations that were used in analyzing the internal wave field are given below. The frequency spectra of vertical displacement (S_ζ) and of clockwise and counterclockwise rotary velocity (S_- and S_+, respectively) consistent with GM79 [*Munk*, 1981] are

$$S_\zeta(\omega) = r\frac{2f}{\pi N(z)}\frac{(\omega^2 - f^2)^{1/2}}{\omega^3} \qquad \text{(A1)}$$

$$S_{\pm}(\omega) = r\frac{fN(z)}{\pi}\frac{(\omega \mp f)^2}{\omega^3(\omega^2 - f^2)^{1/2}} \quad \text{(A2)}$$

The units of S_ζ and $S_\pm$ are $m^2\ s^{-1}$ and $(m\ s^{-1})^2\ s^{-1}$, respectively. The corresponding vertical velocity spectrum is given by

$$S_w(\omega) = \omega^2 S_\zeta(\omega) \quad \text{(A3)}$$

A modified version of the spectra $\hat{S}$ [*Levine et al.*, 1986], where the frequency spectral slope is treated as a free parameter, is given below for an $\omega^{-3/2}$ dependence at high frequency:

$$\hat{S}_\zeta(\omega) = r\frac{f^{1/2}}{N(z)J}\frac{(\omega^2 - f^2)^{1/2}}{\omega^{5/2}} \quad \text{(A4)}$$

$$\hat{S}_\pm(\omega) = r\frac{f^{1/2}N(z)}{J}\frac{(\omega \mp f)^2}{\omega^{5/2}(\omega^2 - f^2)^{1/2}} \quad \text{(A5)}$$

where the nondimensional normalization constant J is given by

$$J = \int_1^{N/f} \frac{d\Omega}{\Omega^{1/2}(\Omega^2 - 1)^{1/2}} \quad \text{(A6)}$$

where Ω is the nondimensional frequency ω/f.

The wave number spectrum can be expressed as [*Levine*, 1990]

$$S_\zeta(\beta) = \int_f^N \left[\frac{2}{\pi}\frac{\beta_*}{(\beta_*^2 + \beta^2)}\right] S_\zeta(\omega)\, d\omega \quad \text{(A7)}$$

$$S_\zeta(\beta) \approx \frac{rt}{\pi}\frac{1}{(\beta_*^2 + \beta^2)}$$

where $\beta_* \equiv tN(z)$ and the factor [ ] is the distribution in wave number and is normalized such that

$$\int [\ ]\, d\beta \simeq 1$$

The wave number spectrum for the modified spectrum $\hat{S}_\zeta(\beta)$ has the same form as (A7):

$$\hat{S}_\zeta(\beta) \simeq 1.24\frac{rt}{\pi}\frac{1}{\beta_*^2 + \beta^2} \quad \text{(A8)}$$

The vertical coherence depends only on t and can be written as [*Desaubies*, 1976]

$$C_\zeta(\Delta z) = \exp[-tN\,\Delta z] \quad \text{(A9)}$$

Acknowledgments. We thank Arnold Gordon for providing CTD data, Roger Andersen for installing the POP buoy and performing the buoy data analysis programming, John Gunn and Mark Morehead for current meter deployment and recovery, Richard Dewey for performing the tidal analysis, Walt Waldorf and Robin Robertson for assistance with MDR and RSVP deployment and data analysis, and Steve Gard for data analysis. This work was supported by the National Science Foundation, Office of Polar Programs, through grants DPP-9024695 and OPP-9317319 to OSU (LP and MDL), OPP-9024828 to SAIC (RDM), and DPP-9100423 and OPP-9410849 to UW (JHM). Ben Connell worked on the initial tidal studies under the Research Experience for Undergraduate Students program (OPP-9347600). The detailed comments by two anonymous reviewers are much appreciated.

References

Armi, L., Some evidence for boundary mixing in the deep ocean, *J. Geophys. Res., 83*, 1971–1979, 1978.

Briscoe, M.G., Preliminary results from the tri-moored internal wave experiment (IWEX), *J. Geophys. Res., 80*, 3872–3884, 1975.

D'Asaro, E.A., and J.H. Morison, Internal waves and mixing in the Arctic Ocean, *Deep Sea Res., Part A, 39*, S459–S484, 1992.

Desaubies, Y.J.F., Analytical representation of internal wave spectra, *J. Phys. Oceanogr., 6*, 976–981, 1976.

Desaubies, Y.J.F., and M.C. Gregg, Reversible and irreversible finestructure, *J. Phys. Oceanogr., 11*, 541–556, 1981.

Egbert, G.D., A.F. Bennett, and M.G.G. Foreman, TOPEX/POSEIDON tides estimated using a global inverse model, *J. Geophys. Res., 99*, 22,821–24,852, 1994.

Fahrbach, E., G. Rohardt, M. Schroder, and V. Strass, Transport and structure of the Weddell Gyre, *Ann. Geophys., 12*, 840–855, 1994.

Foldvik, A., and T. Gammelsrød, Notes on Southern Ocean hydrography, sea-ice and bottom water formation, *Palaeogeogr. Palaeoclimatol. Palaeoecol., 67*, 3–17, 1988.

Foreman, M.G.G., Manual for tidal currents analysis and prediction, *Pac. Mar. Sci. Rep. 78-6*, Inst. of Ocean Sci., Sidney, B.C., Canada, 1978.

Foster, T.D., A. Foldvik, and J.H. Middleton, Mixing and bottom water formation in the shelf break region of the southern Weddell Sea, *Deep Sea Res., Part A, 34*, 1771–1794, 1987.

Gargett, A.E., and J.N. Moum, Mixing efficiencies in turbulent tidal fronts: Results from direct and indirect measurements of density flux, *J. Phys. Oceanogr., 25*, 2583–2608, 1995.

Garrett, C.J., and W. Munk, Space-time scales of internal waves, *Geophys. Astrophys. Fluid Dyn., 2*, 255–264, 1972.

Garrett, C.J., and W. Munk, Space-time scales of internal waves: A progress report, *J. Geophys. Res., 80*, 291–297, 1975.

Genco, M.L., F. Lyard, and C. Le Provost, The oceanic tides in the South Atlantic Ocean, *Ann. Geophys., 12*, 868–886, 1994.

Gordon, A.L., and Ice Station Weddell Group of Principal Investigators and Chief Scientists, Weddell Sea exploration from Ice Station, *Eos Trans. AGU, 74*, 121, 124–126, 1993a.

Gordon, A.L., B.A. Huber, H.H. Hellmer, and A. Ffield, Deep and bottom water of the Weddell Sea's western rim, *Science, 262*, 95–97, 1993b.

Gregg, M.C., A comparison of finestructure spectra from the main thermocline, *J. Phys. Oceanogr., 7*, 33–40, 1977.

Gregg, M.C., Scaling turbulent dissipation in the thermocline, *J. Geophys. Res., 94*, 9686–9698, 1989.

Gregg, M.C., and E. Kunze, Shear and strain in Santa Monica Basin, *J. Geophys. Res., 96*, 16,709–16,719, 1991.

Henyey, F.S., J. Wright, and S.M. Flatté, Energy and action flow through the internal wave field: An eikonal approach, *J. Geophys. Res., 91*, 8487–8495, 1986.

Ivey, G.N., The role of boundary mixing in the deep ocean, *J. Geophys. Res., 92*, 11,873–11,878, 1987.

Katz, E.J., and M.G. Briscoe, Vertical coherence of the internal wave field from towed sensors, *J. Phys. Oceanogr., 9*, 518–530, 1979.

LaBrecque, J.L., and M.E. Ghidella, Estimates of bathymetry, depth to magnetic basement, and sediment thickness for the western Weddell Basin, *Antarct. J. U.S., 27*, 68–70, 1993.

Ledwell, J.R., A.J. Watson, and C.S. Law, Evidence for slow mixing across the pycnocline from an open-ocean tracer-release experiment, *Nature, 364*, 701–703, 1993.

Levine, M.D., Internal waves under the Arctic pack ice during the Arctic Internal Wave Experiment: The coherence structure, *J. Geophys. Res., 95*, 7347–7357, 1990.

Levine, M.D., and J.D. Irish, A statistical description of temperature finestructure in the presence of internal waves, *J. Phys. Oceanogr., 11*, 676–691, 1981.

Levine, M.D., R.A. deSzoeke, and P.P. Niiler, Internal waves in the upper ocean during MILE, *J. Phys. Oceanogr., 13*, 240–257, 1983.

Levine, M.D., C.A. Paulson, and J.H. Morison, Internal waves in the Arctic Ocean: Comparison with lower-latitude observations, *J. Phys. Oceanogr., 15*, 800–809, 1985.

Levine, M.D., J.D. Irish, T.E. Ewart, and S.A. Reynolds, Simultaneous spatial and temporal measurements of the internal wave field during MATE, *J. Geophys. Res., 91*, 9709–9719, 1986.

Levine, M.D., C.A. Paulson, and J.H. Morison, Observations of internal gravity waves under the Arctic pack ice, *J. Geophys. Res., 92*, 779–782, 1987.

Lien, R.-C., and P. Müller, Consistency relations for gravity and vortical modes in the ocean, *Deep Sea Res., Part A, 39*, 1595–1612, 1992.

Lytle, V.I., and S.F. Ackley, Heat flux through sea ice in the western Weddell Sea: Convective and conductive transfer processes, *J. Geophys. Res., 101*, 8853–8868, 1996.

McComas, C.H., and P. Müller, The dynamic balance of internal waves, *J. Phys. Oceanogr., 11*, 970–986, 1981.

McPhee, M.G., Analysis and prediction of short-term ice drift, *J. Offshore Mech. Arctic Eng., 110*, 94–100, 1988.

McPhee, M.G., and L.H. Kantha, Generation of internal waves by sea ice, *J. Geophys. Res., 94*, 3287–3302, 1989.

McPhee, M.G., and D.G. Martinson, Turbulent mixing under drifting pack ice in the Weddell Sea, *Science, 263*, 219–220, 1994.

Middleton, J.H., and T.D. Foster, Fine structure measurements in a temperature-compensated halocline, *J. Geophys. Res., 85*, 1107–1122, 1980.

Middleton, J.H., T.D. Foster, and A. Foldvik, Diurnal shelf waves in the southern Weddell Sea, *J. Phys. Oceanogr., 17*, 784–791, 1987.

Morison, J.H., C.E. Long, and M.D. Levine, Internal wave dissipation under sea ice, *J. Geophys. Res., 90*, 11,959–11,966, 1985.

Muench, R.D., and A.L. Gordon, Circulation and transport of water along the western Weddell Sea margin, *J. Geophys. Res., 100*, 18,503–18,516, 1995.

Müller, P., D.J. Olbers, and J. Willebrand, The IWEX spectrum, *J. Geophys. Res., 83*, 479–500, 1978.

Munk, W., Internal waves and small-scale processes, in *Evolution of Physical Oceanography*, edited by B.A. Warren and C. Wunsch, pp. 264–290, MIT Press, Cambridge, Mass., 1981.

Nøst, E., Calculating tidal current profiles from vertically integrated models near the critical latitude in the Barents Sea, *J. Geophys. Res., 99*, 7885–7901, 1994.

Osborn, T.R., Estimates of the local rate of vertical diffusion from dissipation measurements, *J. Phys. Oceanogr., 10*, 83–89, 1980.

Padman, L., Small-scale processes in the Arctic Ocean, in *Arctic Oceanography: Marginal Ice Zones and Continental Shelves, Coastal and Estuarine Stud.*, vol. 49, edited by W.O. Smith Jr. and J.M. Grebmeier, pp. 97–129, AGU, Washington, D.C., 1995.

Padman, L., and T.M. Dillon, Turbulent mixing near the Yermak Plateau during the Coordinated Eastern Arctic Experiment, *J. Geophys. Res., 96*, 4769–4782, 1991.

Padman, L., A.J. Plueddemann, R.D. Muench, and R. Pinkel, Diurnal tides near the Yermak Plateau, *J. Geophys. Res., 97*, 12,639–12,652, 1992.

Plueddemann, A.J., Internal wave observations from the Arctic Environmental Drifting Buoy, *J. Geophys. Res., 97*, 12,619–12,638, 1992.

Polzin, K.L., J.M. Toole, and R.W. Schmitt, Finescale parameterizations of turbulent dissipation, *J. Phys. Oceanogr., 25*, 306–328, 1995.

Rayleigh, L., Investigation of the character of the equilibrium of an incompressible heavy fluid of variable density, *Proc. London Math. Soc., 14*, 170–178, 1888.

Robertson, R., L. Padman, and M.D. Levine, Finestructure, microstructure and vertical mixing in the upper ocean in the western Weddell Sea, *J. Geophys. Res., 100*, 18,517–18,536, 1995.

Robertson, R.A., G.D. Egbert, and L. Padman, Tidal currents in the Weddell Sea, *Eos Trans. AGU, 77*(3), Ocean Sci. Meet. Suppl., OS86, 1996.

Rubenstein, D., A spectral model of wind-forced internal waves, *J. Phys. Oceanogr., 24*, 819–831, 1994.

Saint-Guily, B., Sur la propagation des ondes de seconde classe le long d'un talus continental, *C.R. Acad. Sci., Ser. B, 282*, 141–144, 1976.

Steele, M. and J.H. Morison, Obtaining smooth hydrographic profiles from a buoy deployed in sea ice, *J. Oceanic Atmos. Technol., 9*, 812–826, 1992.

Stokes, G.G., On the theory of oscillating waves, *Trans. Cambridge Philos. Soc., 8*, 441–455, 1847.

Welander, P., An advective model of the ocean thermocline, *Tellus, 11*, 309–318, 1959.

Wijesekera, H., L. Padman, T. Dillon, M. Levine, C. Paulson, and R. Pinkel, The application of internal-wave dissipation models to a region of strong mixing, *J. Phys. Oceanogr., 23*, 269–286, 1993.

Wunsch, C., Deep ocean internal waves: What do we really know?, *J. Geophys. Res., 80*, 339–343, 1975.

M. D. Levine and L. Padman, College of Oceanic and Atmospheric Science, Oregon State University, 104 Ocean Administration Building, Corvallis, OR 97331. (e-mail: levine@oce.orst.edu; padman@oce.orst.edu)

J H. Morison, Polar Science Center, Applied Physics Laboratory, College of Ocean and Fishery Sciences, University of Washington, 1013 N.E. 40th Street, Seattle, WA 98105. (e-mail: morison@apl.washington.edu)

R. D. Muench, Earth and Space Research, 1910 Fairview East #102, Seattle, WA 98102. (e-mail: rmuench@esr.org)

(Received January 31, 1996; revised September 3, 1996; accepted September 9, 1996.)